Journal of Materials Chemistry A

Accepted Manuscript

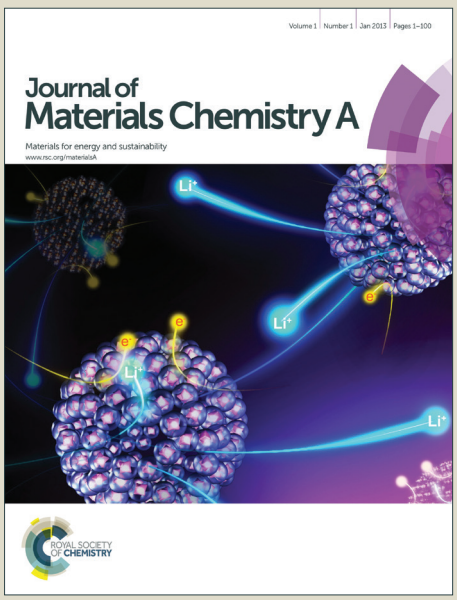

ROYAL SOCIETY OF CHEMISTRY

www.rsc.org/materialsA

Cite this: DOI: 10.1039/c0xx00000x

www.rsc.org/xxxxxx

ARTICLE TYPE

Role of graphene on the band structure and interfacial interaction of Bi_2WO_6/graphene composites with enhanced photocatalytic oxidation of NO

Ying Zhou [a,b*], Xiaojing Zhang [b], Qian Zhang [b], Fan Dong [c*], Fang Wang [b], and Zhuo Xiong [b]

Received (in XXX, XXX) Xth XXXXXXXXX 20XX, Accepted Xth XXXXXXXXX 20XX
DOI: 10.1039/b000000x

Abstract: The photocatalytic performances of Bi_2WO_6 were limited by the slow electron transfer and fast charge recombination. In this report, Bi_2WO_6/graphene (2 wt%) composites were fabricated by a two-step approach using graphene as precursor, which can maintain the crystallinity, morphology and particle size of pristine hierarchical Bi_2WO_6 microspheres, providing the unique opportunities to correlate interfacial interaction to the photocatalytic activity. The interfacial electronic interaction between Bi_2WO_6 and graphene evidenced by X-ray photoelectron spectroscopy (XPS) resulted in positive shifting of the Fermi level and broadening the valence band (VB) of Bi_2WO_6. These reveal a stronger oxidative power and faster mobility of photogenerated holes upon excitation in combination with radical trapping and electron spin resonance (ESR) experiments providing clear evidence for this key property. Compared to pristine Bi_2WO_6, the composites exhibited not only higher photocatalytic activity toward the oxidation of NO, but also better selectivity for the formation of ionic species (NO_3^-) as well as a 9-fold enhancement of the photocurrent density. The significantly improved charge separation and migration in Bi_2WO_6/graphene composite was demonstrated by electrochemical impedance spectroscopy (EIS). Moreover, the interfacial electron transfer rate determined for the composite was 7.97×10^8 s^{-1} through time-resolved fluorescence decay spectra. It was therefore proposed that the enhanced photocatalytic activity of Bi_2WO_6/graphene could be directly ascribed to the deeper VB edge position as well as efficient charge transfer across the interface. The present study points out the key role of graphene in tuning electronic structure and interfacial charge transfer processes for the development of highly efficient photocatalysts.

1. Introduction

In the past few decades, photocatalytic solar-energy conversion has attracted extensive interests due to the increasingly serious energy crisis and environmental pollution.[1-5] The quest for highly efficient photocatalysts is crucial to enable their practical use, which is mainly dictated to three processes: optical absorption, charge separation and migration, and catalytic reaction on surfaces.[6] Among the various studied photocatalysts, Bi_2WO_6 with corner-sharing WO_6 octahedrons sandwiched between $(Bi_2O_2)^{2+}$ layers has been regarded as an excellent photocatalyst due to its intrinsic chemical and physical properties.[7-9] Generally, Bi_2WO_6 can produce O_2 from $AgNO_3$ solution,[10] degrade organic pollutants[7] and reduce CO_2 into hydrocarbon fuels[11] under light irradiation. However, the slow electron transfer and fast charge recombination in Bi_2WO_6 greatly restricted its extended practical applications in photocatalysis.

On the other hand, graphene possess excellent electron transfer properties with a charge transfer mobility of 250 000 cm^2 V^{-1} s^{-1} at room temperature.[12] Apart from its unique electronic properties, graphene have a large surface area (theoretical value ~2600 m^2 g^{-1}) and flexible structure.[13] These unusual properties make it be a suitable candidate to couple with Bi_2WO_6 and improve charge separation and transfer behaviours of Bi_2WO_6. Recently, several studies have clearly demonstrated the enhancement of photocatalytic activity of Bi_2WO_6 with the introduction of graphene.[14-18] For instance, Wang's group reported that graphene/Bi_2WO_6 showed enhanced photocatalytic activity for the degradation of Rhodamine B (RhB), which was attributed to the negative shift in the Fermi level of composites and the high migration efficiency of photoinduced electrons.[14] Along these lines, Min et al. observed a three times enhancement in the photodegradation of RhB over Bi_2WO_6/graphene in comparison with neat Bi_2WO_6.[18] Most recently, a sonochemical method was developed for fabrication of Bi_2WO_6/graphene composite which exhibited higher photocatalytic activities for both H_2 and O_2 generation under visible-light irradiation.[15] Nevertheless, the reported synthetic approaches usually used graphene oxide (GO) as precursor to prepare of Bi_2WO_6/graphene composites through one-step route, in which the crystallinity, morphology and particle size of pristine Bi_2WO_6 may change during the composite formation process.[14-18] Particularly, the photocatalytic reaction process is a complex interplay of each property which is related to each other. Therefore, in practice, the enhanced photocatalytic performance is difficult to attribute to the change of Bi_2WO_6

itself during the reduction of GO or the interaction between Bi_2WO_6 and graphene. Moreover, although several work proposed that the high conductivity of graphene could improve the photogenerated charge separation and transfer in Bi_2WO_6, no direct evidence has been provided.[16-18]

In addition, the previous studies have focused on the photodegradation of organic dyes such as RhB, methyl orange (MO), methylene blue (MB) or water splitting.[14-18] On the other hand, with the development of modern industry, gas pollution is becoming a serious issue which is harmful for human health. In particular, NO is one of the common air pollutions and responsible for many hazardous effects such as global warming, tropospheric ozone, acid rains, human diseases and so on.[19] Photocatalysis is a promising method to remove NO among the proposed strategies.[20] Huang and co-workers found that Bi_2WO_6 can oxidize NO under light irradiation and a higher surface area leads to the improvement of photocatalytic activity.[21] Nevertheless, to the best of our knowledge, there is no research focusing on the photocatalytic oxidation of NO over Bi_2WO_6/graphene composites.

Following our previous work on the understanding of the hydrothermal growth mechanisms of hierarchical Bi_2WO_6 microspheres,[22-23] in the current work, Bi_2WO_6/graphene composites were synthesized by a two-step method using graphene as precursor, which can maintain the crystallinity, morphology and particle size of pristine hierarchical Bi_2WO_6 microspheres. The obtained Bi_2WO_6/graphene (2 wt%) composites exhibited both higher photocatalytic NO oxidation activities and improved selectivity for the formation of ionic species (NO_3^-). X-ray photoelectron spectroscopy (XPS) investigations indicated that the electronic interfacial interaction between Bi_2WO_6 and graphene made the valence band (VB) and conduction band (CB) of Bi_2WO_6 more positive, as well as broadening the VB. The improved transport of photocarriers over Bi_2WO_6/graphene composites has been clearly demonstrated by the photoelectrochemical (PEC) measurements and ns-level time-resolved fluorescence spectra. On the basis of these results, a mechanism for enhanced photocatalytic performances over Bi_2WO_6/graphene was proposed.

2. Experimental

2.1 Materials

All the chemicals were analytical grade reagents and used without any further purification. Graphene was purchased from Sichuan Jinlu Co., Ltd. Deionized water was used in all experiments.

2.2 Synthesis of hierarchical Bi_2WO_6 microspheres

Hierarchical Bi_2WO_6 microspheres were prepared via a hydrothermal method according to our previous work.[24] 0.25 mmol $Na_2WO_4 \cdot 2H_2O$ and 0.5 mmol of $Bi(NO_3)_3 \cdot 5H_2O$ were placed into 25 mL of 20 vol% acetic acid and stirred magnetically for 20 min. Then, the suspension was transferred into a 50 mL Teflon-lined stainless steel autoclave, which was maintained at 160 ◦C for 24 h, and subsequently cooled to room temperature. The precipitate was collected after filtration, washed with distilled water and dried in the air.

2.3 Synthesis of Bi_2WO_6/graphene composites

300 mg of synthesized Bi_2WO_6 powders were dispersed in 84 mL ethanol and 6 mg of graphene (2 wt%) were dispersed in 6 mL ethylene glycol under ultrasonic condition for 30 min, respectively. After that, the graphene were added into the Bi_2WO_6 for further ultrasonification of 30 min. Then the mixture was stirred for 24 h at room temperature. Finally, the precipitate was collected after filtration, washed with ethanol and dried in the air.

2.4 Characterization

Powder X-ray diffraction (PXRD) was performed with a PANalytical X'pert diffractometer operated at 40 kV and 40 mA using Cu K_α radiation. Scanning electron microscopy (SEM) was performed on a Hitachi S-4800 microscope. Transmission electron microscopy (TEM) images were recorded on a FEI Tecnai G2 20 microscope operated at 200 kV. XPS measurements were conducted on a Thermo ESCALAB 250Xi and the binding energies were referenced to the C1s to 284.6 eV. Diffuse reflectance spectra (DRS) data were recorded on a Shimadzu UV-2600 spectrophotometer equipped with an integrating sphere using $BaSO_4$ as the reflectance standard sample. Time-resolved fluorescence decay spectra were recorded at room temperature with a fluorescence spectrophotometer (Edinburgh Instruments, FLSP-920). Electron spin resonance (ESR) signals of radicals spin-trapped by 5,5-dimethy1-1-pyrroline N oxide (DMPO) were recorded at room temperature on a JES FA200 spectrometer. Samples for ESR measurement were prepared by mixing the samples in a 40 mM DMPO solution tank (aqueous dispersion for DMPO-•OH and methanol dispersion for DMPO-•O_2^-) and they were irradiated with an ultraviolet-visible light lamp.

2.5 Photoelectrochemical and photocatalytic measurements

PEC measurements were conducted in a three electrode system on a CH660D electrochemical work station, using the Bi_2WO_6, graphene or Bi_2WO_6/graphene films as the working electrode, saturated calomel electrode (SCE) as the reference electrode, and Pt wire as the counter electrode. All potentials are quoted with respect to SCE. The wavelength range of the lamp used for PEC tests is from 375 to 550 nm. The photocurrent-time dependent experiments of graphene, Bi_2WO_6 and Bi_2WO_6/graphene films at open circuit potential (OCV) was measured in 0.5 M Na_2SO_4 under chopped illumination with 20 s light on/off cycles. The working electrodes were prepared by deposition powders onto conducting glass supports (fluorine-doped tin oxide (FTO) substrate) with a size of 1 cm × 1 cm: 100 mg of samples were suspended in 0.5 mL of dimethylfomamide (DMF) to produce a slurry by grinding for 30 min, then the slurry was coated on the FTO by a scraper with a scale of 50 μm, and subsequently treated at 170◦C for 2 hours. The photocatalytic activities of these samples were evaluated by removing NO at ppb level in a

continuous flow reactor. Details of the reactor setup have been reported in previous studies.[25] A tungsten halogen lamp (150 W) was vertically placed 20 cm above the reactor. The as-prepared sample (200 mg) was dispersed in distilled water (50 ml) by ultrasonic treatment for 10 min, and then coated onto two glass dishes with a diameter of 12.0 cm. The NO gas was acquired from a compressed gas cylinder at a concentration of 100 ppm of NO (N_2 balance, BOC gas) with traceable National Institute of Standards and Technology (NIST) standard. The initial concentration of NO was diluted to about 600 ppb by the air stream. The air stream flow rate and NO were controlled at 2.4 L/min and 15 mL/min, respectively. After the adsorption-desorption equilibrium was achieved, the lamp was turned on. The concentration of NO was measured by a NO_x analyzer (Thermo Scientific, 42i-TL). The removal ratio (η) of NO was calculated by η (%) = $(1 - C/C_0) \times 100\%$, where C is the outlet concentration of NO after reaction for time t and C_0 represents the inlet concentration after achieving adsorption-desorption equilibrium.

3. Results and Discussion

3.1 Structure and morphology of Bi_2WO_6/graphene composites

The PXRD patterns of the pristine Bi_2WO_6 and Bi_2WO_6/graphene composite are shown in Figure 1. All of the diffraction peaks from Bi_2WO_6/graphene are nearly identical to those of orthorhombic Bi_2WO_6 (JCPDS 39-0256). This, therefore, indicates that the structure, crystallinity and crystal orientations of Bi_2WO_6 in composite are not changed and no other impurities are observed. Moreover, no characteristic diffraction peaks of graphene are observed in Bi_2WO_6/graphene which is probably due to the relatively low content (2 wt%) of graphene.[14, 18]

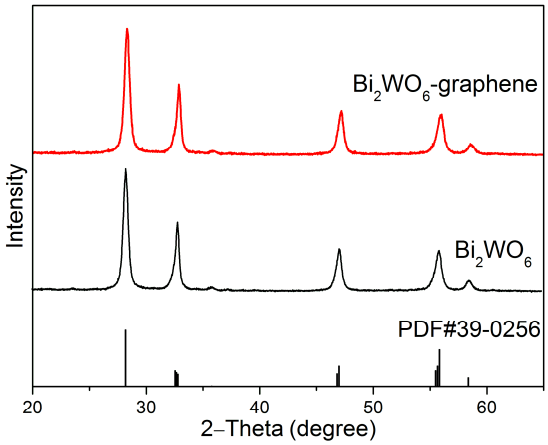

Figure 1. PXRD patterns of pristine Bi_2WO_6 and Bi_2WO_6/graphene composite. The reference pattern of orthorhombic Bi_2WO_6 (JCPDS No. 39-0256) is shown at the bottom.

The SEM images of Bi_2WO_6 and Bi_2WO_6/graphene are shown in Figure 2. Pristine Bi_2WO_6 displays a hierarchical morphology constructed from nanosheet building blocks (Figure 2a), in accord with our previous work.[24] After introducing graphene into the preparation process, the Bi_2WO_6 microspheres can still maintain their hierarchical morphology (Figure 2b). Furthermore, stratiform graphene sheets can also be observed other than Bi_2WO_6 microspheres (Figure 2b-d). The hybridization of Bi_2WO_6 and graphene is further investigated by TEM. The graphene sheets and Bi_2WO_6 spheres are clearly observed in Figure 3a. The obtained particles can be undoubtedly identified as orthorhombic Bi_2WO_6 from their characteristic (131), (002) and (260) reflections in the selected area electron diffraction (SAED) pattern (inset of Figure 3b). The high resolution TEM (HRTEM) image (Figure 3b) shows the crystal lattices of Bi_2WO_6, indicating that the composite is well crystallized. The observed lattice fringes with d spacing of ca. 0.272 nm and 0.315 nm can be assigned to (002) and (131) lattice planes of Bi_2WO_6 respectively, which is consistent with the results from SAED pattern (inset of Figure 3b). All in all, the PXRD, SEM as well as TEM investigations revealed that the crystallinity, morphology and particle size of pristine Bi_2WO_6 can keep almost unchanged after coupling with graphene, which permits the unambiguous correlation of the photocatalytic activity with the modifications through the introduction of graphene.

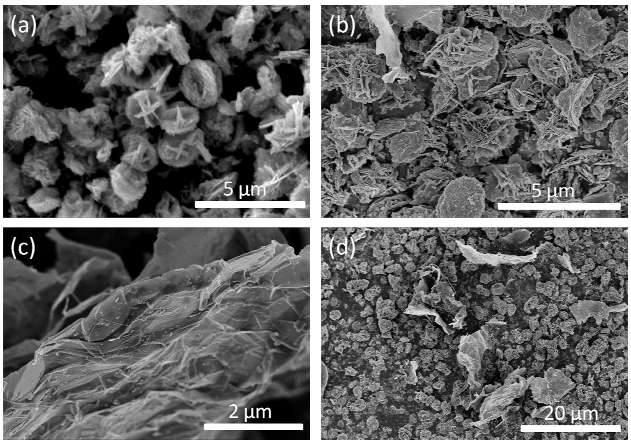

Figure 2. SEM images of Bi_2WO_6 (a) and Bi_2WO_6/graphene (b c d) under different magnifications

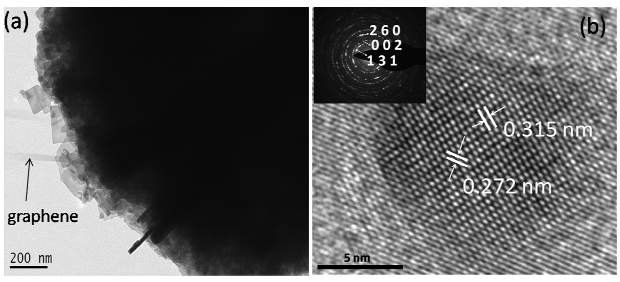

Figure 3. TEM (a) and HRTEM (b) images of Bi_2WO_6/graphene (inset in (b): SAED pattern of Bi_2WO_6/graphene)

3.2 Photocatalytic activities

The photocatalytic activities of Bi_2WO_6 and Bi_2WO_6/graphene were evaluated for the photooxidation of NO at the indoor air

level. Prior to the light irradiation, the adsorption/desorption equilibrium between NO and photocatalysts had been reached. Figure 4a shows the decomposition of NO concentration (C/C_0 %) with irradiation time over Bi_2WO_6 and Bi_2WO_6/graphene under ultraviolet-visible light irradiation. NO is very stable and cannot be photolyzed under light irradiation in the absence of photocatalysts. In the presence of photocatalysts, NO could react with the photogenerated reactive radicals and produce NO_2 intermediate and ionic species, involving four possible reactions as following.[25]

$$NO + 2\cdot OH \rightarrow NO_2 + H_2O \quad (1)$$

$$NO_2 + \cdot OH \rightarrow NO_3^- + H^+ \quad (2)$$

$$NO + NO_2 + H_2O \rightarrow 2HNO_2 \quad (3)$$

$$NO + \cdot O_2^- \rightarrow NO_3^- \quad (4)$$

As shown in Figure 4a, the NO concentration over both Bi_2WO_6 and Bi_2WO_6/graphene decreased rapidly through photocatalytic oxidation within 5 min. After 10 min of irradiation, the removal ratio of NO is 40.0% in the presence of Bi_2WO_6, while an enhanced removal ratio of 59.0% is observed for Bi_2WO_6/graphene. Nevertheless, the NO removal ratio decreased slightly between 5 and 20 min, which could be due to the accumulation of HNO_3 on the photocatalyst surface (cf. Figure 4b),[21] restricting the diffusion of reaction intermediate over materials. This phenomenon can be further observed from the cycling NO oxidation test (Figure S1).[26, 27] The NO removal ratio at the initial time can keep stable over five cycles. After first three runs, the NO removal ratio decreased with the irradiation time, indicating that the accumulation HNO_3 on the photocatalyst surface impaired its activity. Nevertheless, the PXRD pattern investigation of the Bi_2WO_6/graphene composite after cycling tests showed that they did not undergo significant structural changes (Figure S2). Generally, since the reaction intermediate of NO_2 during photocatalytic oxidation of NO is also harmful to human health, the desired oxidation products should be the ionic species (NO_3^-), which can be simply washed away. The ratio of NO_2 in the final oxidation products, on the other hand, is also reflected the photooxidation ability of materials. Therefore, the reaction intermediate of NO_2 is monitored on-line as shown in Figure 4b. After stabilization, the fraction of NO_2 generated over Bi_2WO_6/graphene is as low as 6.4%, which is much lower than that in the presence of Bi_2WO_6 (11.0%). These results indicate that Bi_2WO_6/graphene can promote the oxidation of intermediate NO_2 to final NO_3^- and exhibits stronger oxidation ability in comparison with pure Bi_2WO_6. All in all, Bi_2WO_6/graphene (2 wt%) composites not only show higher photocatalytic NO oxidation activities, but also exhibit improved selectivity for the formation of ionic species.

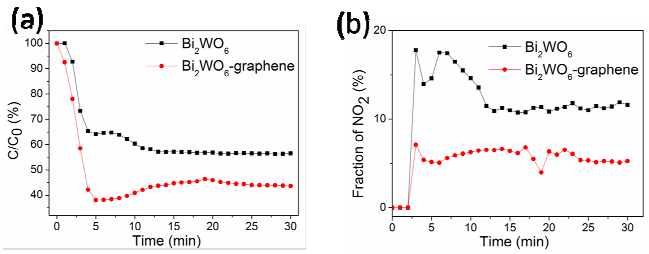

Figure 4. Photocatalytic oxidation of NO (a) and monitoring of the fraction of NO_2 intermediate (b) over Bi_2WO_6 and Bi_2WO_6/graphene under ultraviolet-visible light irradiation

3.3 Optical properties and interfacial interactions

As well known, the photocatalytic activity of semiconductor photocatalysts is intrinsically governed by three processes: light absorption, charge separation and migration, and surface redox potential. In the following, the mechanisms for the enhanced photocatalytic performances of Bi_2WO_6/graphene are explored individually based on the above three processes. The UV-vis DRS of Bi_2WO_6 and Bi_2WO_6/graphene are compared in Figure 5. Bi_2WO_6/graphene (2 wt%) composites exhibit absorption similar to that of pure Bi_2WO_6. The band gaps (E_g) of the Bi_2WO_6 and Bi_2WO_6/graphene were assigned as 3.08 and 3.04 eV, respectively, according to the onset of the absorption edge. Nevertheless, Bi_2WO_6/graphene composites show slight higher absorption intensities than that of Bi_2WO_6 in the visible light region, which could be ascribed to the reintroduction of black body properties of graphite-like materials.[14] Similar phenomenon has been reported by the previous work.[17]

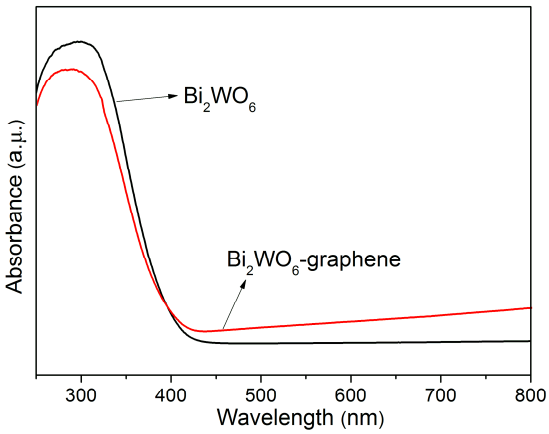

Figure 5. The UV-Vis DRS of Bi_2WO_6 and Bi_2WO_6/graphene

The interactions between the Bi_2WO_6 and graphene in the composites are investigated by XPS spectra. The XPS survey spectra (Figure S3) indicate the presence of Bi, W, O and C in both Bi_2WO_6 and Bi_2WO_6/graphene. Figure 6a-d show the high-resolution spectra of W4f, Bi4f, C1s and O1s, respectively. The peaks with binding energy at 37.3 and 35.1 eV in Bi_2WO_6 corresponding to $W4f_{5/2}$ and $W4f_{7/2}$, respectively, can be assigned to a W^{6+} oxidation state (Figure 6a).[28] Compared to pure Bi_2WO_6, these peaks in Bi_2WO_6/graphene were shifted to 38.0 and 35.9 eV, respectively, indicating the presence of strong interaction between graphene and Bi_2WO_6 microspheres.[15] Note that the similar result was obtained in the binding energies of $Bi4f_{5/2}$ and $Bi4f_{7/2}$. It was observed that the peaks of $Bi4f_{5/2}$ and $Bi4f_{7/2}$ in Bi_2WO_6/graphene were shifted up by 0.7 and 0.6 eV (Figure 6b), respectively, suggesting chemical bonding between Bi_2WO_6 and C elements in graphene.[29] The C1s XPS spectra of Bi_2WO_6

shown in Figure 6c can be devolved into three peaks corresponding to C-C bond (284.6 eV), C-O in epoxy or hydroxyl forms (285.8 eV), and C=O (288.0 eV),[29] respectively, while the peak at 288.0 eV cannot be observed for Bi_2WO_6/graphene, indicating graphene existing in such composites instead of graphene oxide (GO). Compared to Bi_2WO_6, the observed O1s peaks of Bi_2WO_6/graphene also shifted to higher binding energies (Figure 6d), agreeing well with the observations from W4f and Bi4f XPS spectra (Figure 6a and b). All these results clearly demonstrated the strong interfacial interactions between graphene and Bi_2WO_6 microspheres, which could remarkably affect the electronic structures of Bi_2WO_6. As shown in Figure 5, Bi_2WO_6 and Bi_2WO_6/graphene have similar band gap which reveals that the enhanced photocatalytic activity is not mainly attributed to the light absorption. Instead, the band edge potential and charge carrier mobility could play a more important role. Consequently, the X-ray photoelectron VB spectra of Bi_2WO_6 and Bi_2WO_6/graphene are shown in Figure 6e. The VB maximum of Bi_2WO_6 after coupling with graphene is shifted from binding energy of 2.19 to 2.56 eV. Therefore, the VB maximum of Bi_2WO_6/graphene is higher by 0.37 eV, suggesting a much stronger oxidative power of photogenerated holes in the composites. As the VB maximum of anatase TiO_2 is located at +2.64 eV vs. normal hydrogen electrode (NHE) at pH 7,[30] which is 0.64 eV higher than the value obtained by X-ray photoelectron VB spectra, the electronic potentials for Bi_2WO_6 and Bi_2WO_6/graphene were determined at +2.83 and +3.2 eV vs. NHE, respectively. Hence, the band structures of Bi_2WO_6 and Bi_2WO_6/graphene can be drawn and shown in Figure 6f.

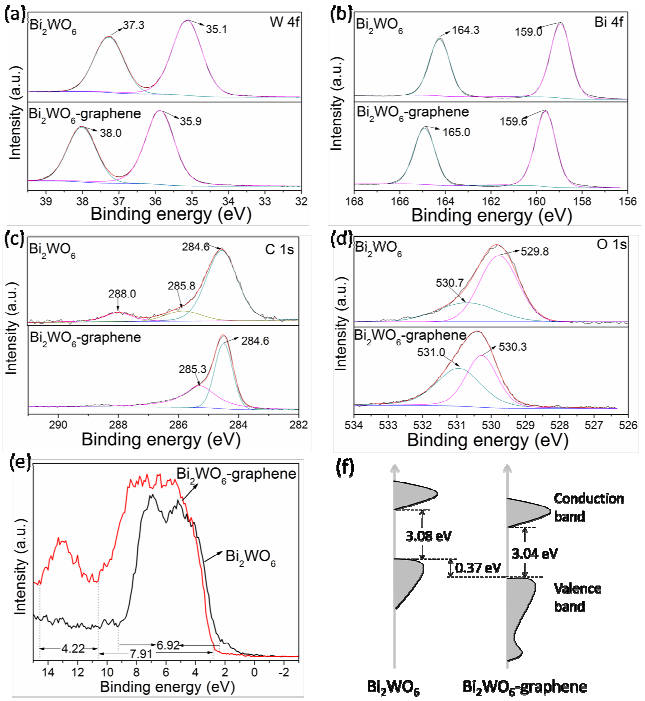

Figure 6. W 4f (a), Bi 4f (b), C 1s (c), O 1s (d) XPS spectra of Bi_2WO_6 and Bi_2WO_6/graphene; valence-band XPS spectra (e) and band structure diagram of Bi_2WO_6 and Bi_2WO_6/graphene (f)

The positive shift in the Fermi level (V_{fb}) of Bi_2WO_6/graphene can be further confirmed by Mott-Schottky (MS) measurements as shown in Figure S4 and Table S1. The chemical interaction between Bi_2WO_6 and graphene can contribute to a 0.34 eV down-shift of V_{fb}, matching well with the results obtained from X-ray photoelectron VB spectra (Figure 6e). In general, the V_{fb} of graphene (-0.08 eV vs. NHE) is more positive than the observed CB of Bi_2WO_6 (-0.25 eV), which means photogenerated electrons can transfer from Bi_2WO_6 to graphene easily once they are in contact. Consequently, the charge equilibration makes the V_{fb} of Bi_2WO_6/graphene shift positively in comparison with that of Bi_2WO_6. Contrarily, both Wang et al. and Sun et al. observed the interaction between graphene and Bi_2WO_6 can lead to the negative shift of V_{fb} in the previous work.[14,15] Such contrary results could be due to the different synthesis approaches. Both of them used GO as precursors which may change the interfacial interactions between Bi_2WO_6 and graphene. In addition, the different synthetic approaches to Bi_2WO_6 could also have influences on the band edge potential of Bi_2WO_6.[14,15] Interestingly, these results point out that both negative and positive shift of VB of Bi_2WO_6 can be achieved through coupling with graphene on the basis of synthetic parameter adjustment. In addition, the valence bandwidth of Bi_2WO_6/graphene is ca. 7.9 eV, which is 1 eV wider than that of Bi_2WO_6 (6.9 eV) due to the possible contributions of C2p and C2s orbitals from graphene.[31] Hence, the wider and more dispersed VB of Bi_2WO_6/graphene could increase the mobility of photogenerated carriers.[32]

It is generally accepted that $\cdot O_2^-$, ·OH and photogenerated h^+ are main reaction species in photocatalytic reactions. Consequently, ESR spin-trap technique with DMPO for both $\cdot O_2^-$ and ·OH is employed to monitor these reaction species. No signals are observed in the darkness (Figure 7). Under light irradiation, DMPO-$\cdot O_2^-$ species were observed for both samples and the intensities of the characteristic peaks of DMPO-$\cdot O_2^-$ increased with the irradiation time (Figure 7a). Nevertheless, the formation rates of $\cdot O_2^-$ radicals on Bi_2WO_6 and Bi_2WO_6/graphene are comparable, indicating the generation ability of $\cdot O_2^-$ radicals did not enhance after coupling with graphene. Surprisingly, the calculated CB minimum of Bi_2WO_6 and Bi_2WO_6/graphene are -0.25 and +0.16 eV vs. NHE, respectively, which are more positive than the standard redox potential of $O_2/\cdot O_2^-$ (-0.28 eV vs. NHE). From the thermodynamics point of view, the photogenerated electrons can not react with the adsorbed O_2 to form $\cdot O_2^-$, but the proposed band structures shown in Figure 6f did not consider the influences of light irradiation which can strongly affect the band structure of materials.[33] Further studies on the exact determination of the band structure upon excitation are currently in progress. No typical signals with characteristic intensity of 1:2:2:1 for DMPO-·OH were observed for both samples no matter the reaction was conducted in darkness or under light irradiation (Figure 7b), suggesting ·OH could not be the dominant photooxidant. Previously, Fu et al. and Wang et al. also reported that ·OH radicals are not the main oxidizing species in the photocatalytic system with Bi_2WO_6.[34] Instead, the hyperfine splitting characteristics of the ESR spectra revealed the direct oxidation of DMPO to DMPOX.[35] Therefore, the direct h^+ oxidation and $\cdot O_2^-$ oxidation reaction could mainly govern the

photocatalytic reactions. Moreover, the formation rates of h^+ on Bi_2WO_6/graphene were much higher than that of pure Bi_2WO_6 (cf. Figure 7b), further confirming the deeper VB edge position and stronger oxidative power in Bi_2WO_6/graphene. Consequently, light absorption is not the dominant factor for their enhanced photocatalytic activity and selectivity toward NO, whilst the positive shift in V_{fb} and wider VB of Bi_2WO_6/graphene play a more important role. Nevertheless, the charge separation and migration processes are still unclear, which will be investigated in the following Part 3.4.

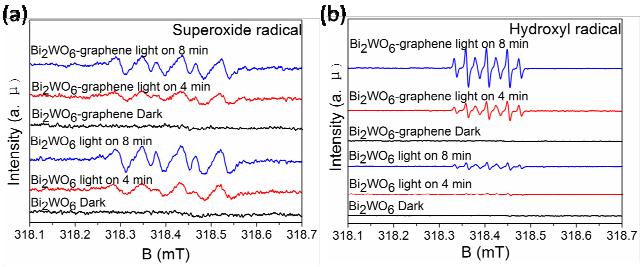

Figure 7. DMPO spin-trapping ESR spectra of Bi_2WO_6 and Bi_2WO_6/graphene in methanol dispersion for DMPO-•O_2^- (a) and in aqueous dispersion for DMPO-•OH (b).

3.4 PEC measurements and time-resolved fluorescence spectra

The transient photocurrent responses for graphene, Bi_2WO_6 and Bi_2WO_6/graphene under ultraviolet-visible light irradiation (with wavelength from 378 to 550 nm) are shown in Figure S5. Almost no photocurrent was observed for pure graphene. It is worth to note that the photocurrent on Bi_2WO_6/graphene is about 9 times higher than that of Bi_2WO_6, which is consistent with the photocatalytic measurements and indicates a much higher efficiency of charge separation as graphene could play a role as an acceptor of the electrons photogenerated over Bi_2WO_6. Electrochemical impedance spectroscopy (EIS) is further used to investigate the photogenerated charge separation process, as shown in Figure 8. The diameter of the arc radius on the EIS Nyquist plot of Bi_2WO_6/graphene is smaller than that of pure Bi_2WO_6 regardless of whether it is in the darkness or under light irradiation, which reveals an effective separation of photogenerated electron-hole pairs and fast interfacial charge transfer to the electron donor or electron acceptor over Bi_2WO_6/graphene in line with the photocurrent measurements.[36] Although graphene possess excellent high conductivity, the diameter of the arc radius on the EIS Nyquist plot of graphene keeps almost unchanged both in the darkness and under light irradiation (cf. Figure S6). Moreover, Figure 8c shows the equivalent circuit model fitted by the obtained data and Table S2 shows the values of fitting circuit. Here, R1 and R2 represent the resistance of the solution and the counter electrode, respectively, which keep almost unchanged with light off and on for both Bi_2WO_6 and Bi_2WO_6/graphene. It is interesting that the resistances of work electrode (R3) are 15191 and 30 Ω for pristine Bi_2WO_6 and Bi_2WO_6/graphene, respectively. These results clearly demonstrated the conductivity of the Bi_2WO_6 is increased of 3 orders of magnitude after coupling with graphene. The high conductivity can facilitate kinetic charge transfer and thus improve the photocatalytic activity as recently demonstrated by Irvine et al. on metallic photocatalysts,[37] and by our group on semimetallic photocatalysts.[38]

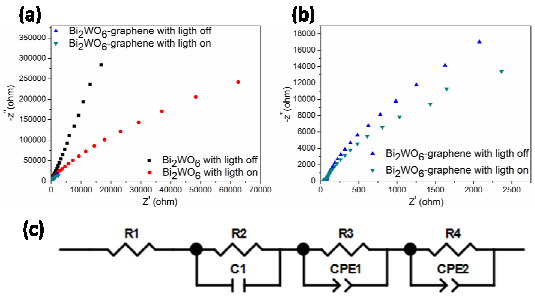

Figure 8. EIS spectra of Bi_2WO_6 and Bi_2WO_6/graphene (a); the magnified EIS spectra of Bi_2WO_6/graphene (b); equivalent circuit constructed from these electrodes (c)

The ns-level time-resolved fluorescence decay spectra were further employed to investigate the charge transfer dynamic over Bi_2WO_6 and Bi_2WO_6/graphene. Figure 9 shows the ns-level time-resolved fluorescence spectra for both samples. The curves can be fitted well based on a biexponential decay function. The fitting parameters are summarized in Table 1. The short lifetime (τ_1) of Bi_2WO_6 is 0.1660 ns. After coupling with graphene, the τ_1 is decreased to 0.1466 ns. The long lifetime (τ_2) of charge carriers is 0.9676 ns for Bi_2WO_6 and 0.9203 ns for Bi_2WO_6/graphene, respectively, confirming the role of graphene in storing and shuttling electrons from photoexcited Bi_2WO_6.[39] Nevertheless, the average life time (τ_{av}) for Bi_2WO_6 and Bi_2WO_6/graphene is 0.4374 and 0.4309 ns, respectively, which are comparable. These results indicated that the coupling of Bi_2WO_6 with graphene did not increase the radiative lifetime of charge carriers, which differs from the introduction of noble-metal in Bi based oxides.[40] In addition, the apparent electron transfer (ET) rate (k_{ET}) in Bi_2WO_6/graphene can be obtained according to the following equation: [41]

$$k_{ET} = \frac{1}{\tau_1(Bi_2WO_6/graphene)} - \frac{1}{\tau_1(Bi_2WO_6)} \quad (5)$$

The calculated value is 7.97×10^8 s^{-1}, which is even larger than that of P25/graphene (1.15×10^8 s^{-1}) and TiO_2 nanotube/graphene (3.47×10^8 s^{-1}),[39] revealing that the formed interface between Bi_2WO_6 and graphene favors effective ET quenching of the excited state of Bi_2WO_6.

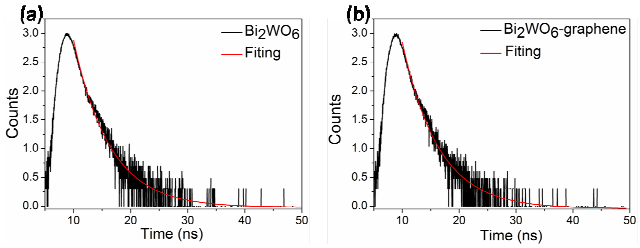

Figure 9. The ns-level time-resolved fluorescence spectra monitored at 505 nm under 380 nm excitation at room temperature for Bi_2WO_6 (a) and Bi_2WO_6/graphene (b)

Table 1. Kinetic parameters of the fitting decay parameters of Bi_2WO_6 and Bi_2WO_6/graphene

Samples	Component	Life time (ns)	Relative Percentage (%)	χ^2
Bi_2WO_6	τ_1	0.1660	66.14	
	τ_2	0.9676	33.86	1.158
	τ_{av}	0.4374	100	
Bi_2WO_6/ graphene	τ_1	0.1466	63.25	
	τ_2	0.9203	36.75	1.053
	τ_{av}	0.4309	100	

Based on the above results, the mechanisms for the enhanced photocatalytic performances toward the oxidation of NO over Bi_2WO_6/graphene composite are proposed as following. Light absorption is not the dominant factor to enhance the photocatalytic activity due to the similar band gap after coupling with graphene. The electronic interfacial interaction between Bi_2WO_6 and graphene can contribute to a 0.36 eV down-shift of VB maximum and 1.0 eV of wider VB, resulting in a much stronger oxidative power of photogenerated holes, which lead to the enhanced generation of reactive oxygen species (h^+) and improved selectivity for the formation of ionic species. In addition, due to the excellent electron mobility of graphene, photogenerated electrons in the excited Bi_2WO_6 can inject rapidly into graphene across the interface which results in the effective charge transfer. Therefore, both the improved charge transfer and surface redox potential lead to the enhanced photocatalytic activity of Bi_2WO_6/graphene composite.

4. Conclusions

In summary, graphene grafted hierarchical Bi_2WO_6 composites were fabricated by a two-step method using graphene as precursor. Compared to pristine hierarchical Bi_2WO_6 microspheres, the composites exhibited both higher photocatalytic removal ratio of NO (59.0%) and better selectivity for the formation of ionic species (93.6%). In addition, the photocurrent density of Bi_2WO_6 was enhanced by a factor of 9 and their conductivity increased of 3 orders of magnitude after coupling with graphene. The electronic interfacial interaction between graphene and Bi_2WO_6 results in a 0.36 eV down-shift of VB maximum and 1.0 eV wider of VB as well as effective charge separation and transfer, which have notable influences on their photocatalytic processes. These results provide fundamental insights into the key role of graphene in tuning electronic structure and interfacial charge transfer processes, which are crucial to fulfil their potential in photocatalysis.

Acknowledgements

Financial support by the National Natural Science Foundation of China (51102245), Sichuan Youth Science and Technology Foundation (2013JQ0034, 2014JQ0017), the Innovative Research Team of Sichuan Provincial Education Department and SWPU (2012XJZT002, KSZ13073), and Scientific Research Starting Project of SWPU (2014QHZ021) is gratefully acknowledged.

Notes and references

[a] *State Key Laboratory of Oil and Gas Reservoir and Exploitation, Southwest Petroleum University, Chengdu 610500, china. Fax: + 86 28 83037406; Tel: +86 28 83037411; E-mail: yzhou@swpu.edu.cn*
[b] *School of Materials Science and Engineering, Southwest Petroleum University, Chengdu 610500, china.*
[c] *College of Environmental and Biological Engineering, Chongqing Technology and Business University, Chongqing 400067, China. E-mail: dfctbu@126.com*

† Electronic Supplementary Information (ESI) available: [Cycling runs of photocatalytic activities for removal of NO in air; XRD patterns of Bi_2WO_6/graphene before and after cycling photocatalytic tests; The XPS survey spectra; MS measurements for Bi_2WO_6 and Bi_2WO_6/graphene; The transient photocurrent responses under ultraviolet-visible light irradiation; EIS spectra of graphene in the darkness and under light irradiation; The fitting values of equivalent circuit model.]. See DOI: 10.1039/b000000x/

1 A. Kudo, Y. Miseki, *Chem. Soc. Rev.*, 2009, **38**, 253.
2 X. H. Gao, H. B. Wu, L. X. Zheng, Y. J. Zhong, Y. Hu, X. W. Lou, *Angew. Chem. Int. Ed.*, 2014, **53**, 5917.
3 X. B. Chen, S. H. Shen, L. J. Guo, S. S. Mao, *Chem. Rev.*, 2010, **110**, 6503.
4 H. Tong, S. Ouyang, Y. P. Bi, N. Umezawa, M. Oshikiri, J. H. Ye, *Adv. Mater.*, 2012, **24**, 229.
5 M. Zhou, X. W. Lou, Y. Xie, *Nano Today*, 2013, **8**, 598.
6 X. B. Chen, L. Liu, P. Y. Yu, S. S. Mao, *Science*, 2011, **331**, 746.
7 M. Ge, Y. F. Li, L. Liu, Z. Zhou, W. Chen, *J. Phys. Chem. C*, 2011, **115**, 5220.
8 L. S. Zhang, W. Z. Wang, L. Zhou, H. L. Xu, *Small*, 2007, **3**, 1618.
9 C. Zhang, Y. F. Zhu, *Chem. Mater.*, 2005, **17**, 3537.
10 K. Kudo, S. Hijii, *Chem. Lett.*, 1999, **10**, 1103.
11 Y. Zhou, Z. P. Tian, Z. Y. Zhao, Q. Liu, J. H. Kou, X. Y. Chen, J. Gao, S. C. Yan, Z. G. Zou, *ACS Appl. Mater. Interfaces*, 2011, **3**, 3594.
12 M. J. Allen, V. C. Tung, R. B. Kaner, *Chem. Rev.*, 2010, **110**,132.
13 S. Stankovich, D. A. Dikin, G. H. B. Dommentt, K. M. Kohlhaas, E. J. Zimney, E. A. Stach, R. D. Piner, S. T. Nguyen, R. S. Ruoff, Materials *Nature*, 2006, **442**, 282.
14 E. Gao, W. Z. Wang, M. Shang, J. H. Xu, *Phys. Chem. Chem. Phys.*, 2011, **13**, 2887.
15 Z. H. Sun, J, J, Guo, S. M. Zhu, L. Mao, J. Ma, D. Zhang, *Nanoscale*, 2014, **6**, 2186.
16 S. M. Sun, W. Z. Wang, L. Zhang, *J. Phys. Chem. C*, 2013, **117**, 9113.
17 J. J. Xu, Y. H. Ao, M. D. Chen, *Mater. Lett.*, 2013, **92**, 126.
18 Y. L. Min, K. Zhang, Y. C. Chen, Y. G. Zhang, *Sep. Purif. Technol.*, 2012, **86**, 98.

19 J, Ângelo, L. Andrade, L. M. Madeira, A. Mendes, *J. Environ. Manag.*, 2013, **129**, 522.

20 F. Dong, Z. W. Zhao, T. Xiong, Z. L. Ni, W. D. Zhang, Y. J. Sun, W. K. Ho, *ACS Appl. Mater. Interfaces*, 2013, **5**, 11392.

21 Y. Huang, Z. H. Ai, W. K. Ho, M. J. Chen, S. C. Lee, *J. Phys. Chem. C*, 2010, **114**, 6342.

22 Y. Zhou, E. Antonova, W. Bensch, G. R. Patzke, *Nanoscale*, 2010, **2**, 2412.

23 Y. Zhou, E. Antonova, Y. H. Lin, J. D. Grunwaldt, W. Bensch, G. R. Patzke, *Eur. J. Inorg. Chem.*, 2012, 783.

24 Y. Zhou, K. Vuille, A. Heel, G. R. Patzke, *Z. Anorg. Allg. Chem.*, 2009, **635**, 1848.

25 W. D. Zhang, Q. Zhang, F. Dong, *Ind. Eng. Chem. Res.*, 2013, **52**, 6740.

26 a) Y. H. Li, J. Xing, Z. J. Chen, Z. Li, F. Tian, L. R. Zheng, H. F. Wang, P. Hu, H. J. Zhao, H. G. Yang, *Nature Commun.*, 2013, **4**, 2500; b) J. Xing, W. Q. Fang, H. J. Zhao, H. G. Yang, *Chem. Asian J.*, 2012, **7**, 642.

27 T.-F. Yeh, C.-Y. Teng, S.-J. Chen, H. Teng, *Adv. Mater.*, 2014, 26, 3297.

28 J. H. Ryu, S. Y. Bang, W. S. Kim, G. S. Park, K. M. Kim, J. Yoon, K. B. Shim, N. Koshizaki, *J. Alloys Compd.*, 2007, **441**, 146.

29 L. H. Tian, J. Y. Liu, C. Q. Gong, L. Q. Ye, L. Zan, *J. Nanopart. Res.*, 2013, **15**, 1917.

30 S. Sakthivel, H. Kisch, *ChemPhysChem*, 2003, **4**, 487.

31 W. Geng, H. X. Liu, X. J. Yao, *Phys. Chem. Chem. Phys.*, 2013, **15**, 6025.

32 R. Shi, G. L. Huang, J. Lin, Y. F. Zhu, *J. Phys. Chem. C*, 2009, **113**, 19633.

33 Q. Zhang, Y. Zhou, W. Li. *In preparation*.

34 a) H. B. Fu, C. S. Pan, W. Q. Yao, Y. F. Zhu, *J. Phys. Chem. B* 2005, **109**, 22432; b) C. Y. Wang, L. Y. Zhu, M. C. Wei, P. Chen, G. Q. Shan, *Water Res.*, 2012, **46**, 845.

35 G. M. Rosen, E. J. Rauckman, *Mol. Pharmacol.*, 1980, **17,** 233.

36 Y. Zhou, Q. Zhang, Y. H. Lin, E. Antonova, W. Bensch, G. R. Patzke, *Sci. China Chem.*, 2013, **56**, 435.

37 X. X. Xu, C. Randorn, P. Efstathiou, J. T. S. Irvine, *Nature Mater.*, 2012, **11**, 595.

38 Q. Zhang, Y. Zhou, F. Wang, F. Dong, W. Li, H. M. Li, G. R. Patzke, *J. Mater. Chem. A*, 2014, **2**, 11065.

39 J. Sun, H. Zhang, L. H. Guo, L. X. Zhao, *ACS Appl. Mater. Interfaces*, 2013, **5**, 13035.

40 F. Dong, Q. Y. Li, Y. Zhou, Y. J. Sun, H. D. Zhang, Z. B. Wu, *Dalton Trans.*, 2014, **43**, 9468.

41 A. Kongkanand, K. Tvrdy, K. Takechi, M. Kuno, P. V. Kamat, *J. Am. Chem. Soc.*, 2008, **130**, 4007.